

# THE RELATION BETWEEN EJECTA VELOCITY, INTRINSIC COLOR, AND HOST-GALAXY MASS FOR HIGH-REDSHIFT TYPE Ia SUPERNOVAE

RYAN J. FOLEY<sup>1,2</sup>

*Draft version August 29, 2018*

## ABSTRACT

Recently, using a large low-redshift sample of Type Ia supernovae (SNe Ia), we discovered a relation between SN Ia ejecta velocity and intrinsic color that improves the distance precision of SNe Ia and reduces potential systematic biases related to dust reddening. No SN Ia cosmological results have yet made a correction for the “velocity-color” relation. To test the existence of such a relation and constrain its properties at high redshift, we examine a sample of 75 SNe Ia discovered and observed by the Sloan Digital Sky Survey-II (SDSS-II) Supernova Survey and Supernova Legacy Survey (SNLS). From each spectrum, we measure ejecta velocities at maximum brightness for the Ca H&K and Si II  $\lambda 6355$  features,  $v_{\text{Ca H\&K}}^0$  and  $v_{\text{Si II}}^0$ , respectively. Using SN light-curve parameters, we determine the intrinsic  $B_{\text{max}} - V_{\text{max}}$  for each SN. Similar to what was found at low-redshift, we find that SNe Ia with higher ejecta velocity tend to be intrinsically redder than SNe Ia with lower ejecta velocity. The distributions of ejecta velocities for SNe Ia at low and high redshift are similar, indicating that current cosmological results should have little bias related to the velocity-color relation. Additionally, we find a slight ( $2.4\text{-}\sigma$  significant) trend between SN Ia ejecta velocity and host-galaxy mass such that SNe Ia in high-mass host galaxies tend to have lower ejecta velocities as probed by  $v_{\text{Ca H\&K}}^0$ . These results emphasize the importance of spectroscopy for SN Ia cosmology.

*Subject headings:* supernovae: general — distance scale — dust, extinction

## 1. INTRODUCTION

Type Ia supernovae (SNe Ia) are reasonable standard candles in the optical, with a dispersion in their peak magnitudes of  $\sim 0.5$  mag (e.g., Baade 1938; Kowal 1968). An empirical relation between the peak luminosity and light-curve shape (Phillips 1993) of a SN Ia combined with accounting for host-galaxy dust extinction (Riess et al. 1996) standardizes SN Ia luminosities such that after corrections, the dispersion in peak magnitudes is  $\sim 0.15$  mag in the optical (e.g., Hicken et al. 2009a). Recently, we discovered that after accounting for the “width-luminosity” relation, low-redshift SNe Ia with higher-velocity ejecta tend to be intrinsically redder than those with lower-velocity ejecta (Foley & Kasen 2011, hereafter FK11), which can improve SN Ia distance precision by a factor of  $\sim 2$ . We also presented a method to correct for this intrinsic color difference when there is a measurement of either the Ca II H&K or Si II  $\lambda 6355$  velocities ( $v_{\text{Ca H\&K}}$  and  $v_{\text{Si II}}$ , respectively) near maximum brightness (Foley et al. 2011, hereafter FSK11), which are proxies for the velocity of all ejecta in the direction of our line of sight. The combination of the width-luminosity and “velocity-color” relations make SNe Ia standardizable candles and crayons.

The distance precision achieved after correcting for light-curve shape and observed color is adequate to determine that the expansion of the Universe is accelerating (Riess et al. 1998; Perlmutter et al. 1999) and constrain the equation-of-state parameter of dark energy,  $w$  (Wood-Vasey et al. 2007; Riess et al. 2007; Hicken et al. 2009b; Kessler et al. 2009; Amanullah et al.

2010; Conley et al. 2011; Sullivan et al. 2011). However, neglecting the relation between ejecta velocity and intrinsic color can potentially bias cosmological results at a level that will significantly bias measurements of  $w$ .

Cosmological parameter measurement with SNe Ia uses differential distance measurements, such that assuming an incorrect SN Ia intrinsic color will not bias results as long as the intrinsic color distribution (and particularly the average) does not change with redshift. If the average intrinsic color changes with redshift, then the color offset will result in an incorrect measurement of host-galaxy extinction, and thus a biased average distance. Since the intrinsic color difference between low and high-velocity SNe Ia is  $\sim 0.1$  mag (FK11), extremely different low and high-redshift populations could result in up to a  $\sim 0.15$  mag bias in distance measurements. Thus far, the velocity-color relation has not been tested at high redshift.

The velocity-color relation is also linked to several aspects of SN explosion physics. First,  $v_{\text{Si II}}$  is strongly correlated with its velocity gradient,  $\dot{v}_{\text{Si II}}$  (FSK11). Maeda et al. (2010) found that  $\dot{v}_{\text{Si II}}$  and velocity offset of nebular lines at late times were correlated, indicating an asymmetric explosion as the origin of the velocity differences. Maeda et al. (2011) found that  $\dot{v}_{\text{Si II}}$  was correlated with intrinsic color, supporting the results of FK11. The polarization of the Si II  $\lambda 6355$  feature, which probes asymmetry in the outer ejecta, is also correlated with velocity (Leonard et al. 2005; Maund et al. 2010). Ganeshalingam et al. (2011) found that SNe Ia with higher-velocity tend to have shorter  $B$ -band rise times than lower-velocity SNe Ia.

In the Chandrasekhar-mass spherically symmetric explosion model, the kinetic energy of the ejecta is proportional to the square of the velocity. More generally, the

<sup>1</sup> Harvard-Smithsonian Center for Astrophysics, 60 Garden Street, Cambridge, MA 02138.

<sup>2</sup> Clay Fellow. Electronic address rfoley@cfa.harvard.edu .

kinetic energy per unit mass is proportional the square of the velocity. However, once spherical symmetry is broken, an additional factor relating the measured velocity to the average velocity is necessary to link kinetic energy and velocity (e.g., Kasen & Plewa 2007). Nonetheless, Velocity information may be an effective way to answer questions about SN Ia progenitor systems and explosion physics. Measuring these properties at high redshift has the potential to provide additional information for understanding SN Ia explosion physics and the progenitor question.

High-redshift SNe Ia are relatively faint, and 8-m class telescopes are typically required to obtain spectra. There are now hundreds of high-redshift SN Ia spectra (e.g., Coil et al. 2000; Hook et al. 2005; Howell et al. 2005; Matheson et al. 2005; Bronder et al. 2008; Ellis et al. 2008; Zheng et al. 2008; Balland et al. 2009; Foley et al. 2009, 2010; Konishi et al. 2011; Östman et al. 2011; Walker et al. 2011). Because of their faintness and the scarcity of large-aperture telescope time, spectral time series of high-redshift SNe Ia are rarely obtained. Previous studies have shown that the ensembles of low and high-redshift SNe Ia have similar spectral evolution (e.g., Blondin et al. 2006; Bronder et al. 2008; Foley et al. 2008). Under the assumption that the low and high-redshift SNe Ia evolve in a similar fashion, a single near-maximum spectrum is adequate to examine the velocity-color relation (FSK11). There have been several high-redshift SN surveys, but to address the velocity-color relation, which is a relatively small effect, it is best to use large, homogeneous samples. It is therefore best to focus on the recent ESSENCE (Miknaitis et al. 2007), Sloan Digital Sky Survey-II Supernovae Survey (SDSS-II; Frieman et al. 2008), and Supernova Legacy Survey (SNLS; Astier et al. 2006) programs.

ESSENCE photometry consists of only two bands, and is therefore not well suited for separating intrinsic color and dust reddening. The current SDSS-II sample is relatively small (only 103 SNe Ia with published light curves), but has excellent multi-band light curves for most SNe and because of its intermediate redshift range ( $z \lesssim 0.4$ ), optical spectra typically cover both Ca H&K and Si II  $\lambda 6355$ . SNLS has a large published sample of light curves (242 SNe Ia with measured light-curve properties) and spectra (330 publicly available spectra). Additionally, the SNLS SN Ia redshift range ( $0.4 \lesssim z \lesssim 1$ ) is higher and complementary to the redshift range of SDSS-II, which could help see any potential redshift evolution in the velocity-color relation.

After correcting for light-curve shape and observed color, SN Ia absolute magnitudes (or equivalently, Hubble residuals) correlate with host-galaxy mass, morphology, and star-formation rate (Hicken et al. 2009b; Kelly et al. 2010; Lampeitl et al. 2010; Sullivan et al. 2010). This empirical relation does not have an understood physical effect, although it could be host-galaxy dust properties, progenitor age, metallicity, or other effects (e.g., Höflich et al. 1998; Lentz et al. 2000; Röpke & Hillebrandt 2004; Mazzali & Podsiadlowski 2006; Conley et al. 2007; Sauer et al. 2008). Since the low and high-redshift host-galaxy populations have different properties (both from selection effects and redshift evolution; Howell et al. 2007), not accounting for

this relation will bias cosmological results (Kelly et al. 2010; Lampeitl et al. 2010; Sullivan et al. 2010).

In this paper, we perform an analysis of the combined SDSS-II and SNLS sample of SNe Ia and compare the sample to the FSK11 low-redshift sample to examine the velocity-color relation at high redshift. After making several practical and quality cuts, we obtain subsamples of the high-redshift sample with appropriate light-curve properties and well-determined maximum-brightness ejecta velocity measurements (Section 2). In Section 3, we measure  $v_{\text{Ca H\&K}}$ ,  $v_{\text{Si II}}$ ,  $v_{\text{Ca H\&K}}^0$ , and  $v_{\text{Si II}}^0$  for the high-redshift sample. In Section 4, we find no difference in the average velocity properties between the low and high-redshift samples; similar to SNe Ia in the low-redshift sample, higher-velocity SNe Ia in the high-redshift sample are observed to be redder than their lower-velocity counterparts; SNe Ia in the high-redshift sample with higher-velocity ejecta tend to be intrinsically redder, confirming the velocity-color relation at high redshift; and there is a marginal trend between ejecta velocity and host-galaxy mass. We summarize and conclude in Section 5.

## 2. SAMPLES

For our study, we use three samples of SNe Ia. The first is the high-redshift SNLS sample; the second is the intermediate-redshift SDSS-II sample. We merge the SDSS-II and SNLS samples to generate our high-redshift sample. The light curves of both the SDSS-II and SNLS samples were fit by Conley et al. (2011), who provide a consistent set of light-curve parameters for all high-redshift SNe. The last sample is the low-redshift sample of FSK11. We discuss the samples and our quality cuts below.

### 2.1. SNLS

With the release of the 3-year SNLS cosmology results (Guy et al. 2010; Conley et al. 2011; Sullivan et al. 2011), the SNLS team also released the one-dimensional spectra for their sample<sup>3</sup>. Most of these spectra have been presented in various publications (Howell et al. 2005; Bronder et al. 2008; Ellis et al. 2008; Balland et al. 2009; Walker et al. 2011); however, several spectra have not been published. Details of the selection, observations, and spectral reductions can be found in the various SNLS spectroscopy references. In total, there are 330 spectra of 316 SNe Ia.

Although the spectroscopic sample is quite large, it must be considerably culled for our study. First, we require light curve information for our study (Guy et al. 2010). Specifically, times of maximum brightness, light-curve shape measurements, and some indication of the SN color are necessary. Many of the spectra are of SNe obtained after year 3 of SNLS, for which there are no published light curves, or have light curves that are not adequate for fitting, and thus do not have corresponding photometric measurements presented by Conley et al. (2011). After matching to the photometry sample, we are left with 212 spectra of 205 SNe Ia, or 85% of the photometry sample.

<sup>3</sup> All spectra can be obtained at <https://tspace.library.utoronto.ca/handle/1807/26549>.

FSK11 was able to correct  $v_{\text{Si II}}$  and  $v_{\text{Ca H\&K}}$  to their maximum-light values,  $v_{\text{Si II}}^0$  and  $v_{\text{Ca H\&K}}^0$ , respectively, if the spectra were obtained near maximum brightness. Specifically, the measurements must be made within  $-6 \leq t \leq 10$  days and  $-4 \leq t \leq 9$  days in the rest frame for  $v_{\text{Si II}}$  and  $v_{\text{Ca H\&K}}$ , respectively. Additionally, FSK11 found that this relation held for SNe Ia with  $1 \leq \Delta m_{15}(B) \leq 1.5$  mag. This light-curve shape constraint was made to properly match the  $\Delta m_{15}(B)$  dispersion for the low-redshift low and high-velocity samples (Wang et al. 2009); however, the velocity relations hold for  $0.9 \leq \Delta m_{15}(B) \leq 1.5$  mag, and we use this range for our analysis to include more SNe. Using Equation 5 of Conley et al. (2008), we can convert the  $\Delta m_{15}(B)$  ranges with minimum values of 1 and 0.9 mag to stretch ranges of  $0.772 \leq s \leq 1$  and  $0.772 \leq s \leq 1.067$ , respectively. After making the phase and light-curve shape cuts, we are left with 106 and 115 spectra of 101 and 110 SNe Ia for  $v_{\text{Ca H\&K}}^0$  and  $v_{\text{Si II}}^0$ , respectively.

Although the SNLS sample of SN Ia spectra is of relatively good quality for high-redshift data, not all spectra are adequate for measuring ejecta velocities. We perform a visual inspection of all spectra to determine their fidelity and reject spectra that are noisy, have large sky residuals, have poor flux calibration, or other obvious problems. In addition, because of the redshift range of the sample and the wavelength range of the spectra, most spectra do not cover Si II  $\lambda 6355$  and some do not cover Ca H&K, thus precluding a measurement of their ejecta velocity from those lines. Finally, we use the criteria determined by FSK11 for determining if a  $v_{\text{Ca H\&K}}$  measurement indicates the true ejecta velocity or that of a high-velocity component and/or blend with another line (e.g., Si II  $\lambda 3858$ ; Kirshner et al. 1993; Nugent et al. 1997; Howell et al. 2006). Specifically, we reject spectra with a visually apparent red shoulder in the line profile and spectra that have both  $f_{\text{Ca}} = f_{\lambda}(v_{\text{Ca H\&K}} + 9000 \text{ km s}^{-1})/f_{\lambda}(v_{\text{Ca H\&K}}) < 1.5$  and  $v_{\text{Ca H\&K}} < -14,000 \text{ km s}^{-1}$ . After making the spectral quality cuts, we are left with 13 and 39 spectra of 13 and 38 SNe Ia for  $v_{\text{Si II}}^0$  and  $v_{\text{Ca H\&K}}^0$ , respectively.

A summary of the cuts and how they affect the sample are presented in Table 1.

After making all cuts, we are left with 4% and 12% of the original sample for analysis of the Si II  $\lambda 6355$  and Ca H&K, respectively. We use 6% and 18% of the sample with photometric measurements. If we assume that photometric measurements will be provided in the future for the remaining sample and that the percentages measured here are representative of the full sample, then we can expect  $\sim 6$  and  $\sim 18$  additional spectra for the two measurements. A summary of the cuts and how they affect the sample are presented in Table 1.

The Si II  $\lambda 6355$  feature is rarely measured for SNe Ia in the SNLS sample. This results in the largest reduction for that feature. Future surveys which find more SNe Ia at  $z < 0.4$  (approximately where the feature is redshifted beyond the optical range) should provide a significant number of SNe Ia where this feature can be observed with optical spectrographs. Alternatively, near-infrared spectroscopy could measure this feature at higher redshift. The number of spectra which pass all Ca H&K cuts is reduced by both the light-curve shape cut and

the quality of the data. Additional investigations of the velocity evolution as a function of light-curve shape may help with the former cut. Longer exposure times for spectral observations (or larger-aperture telescopes) will help with the latter cut.

## 2.2. SDSS-II

SDSS-II have released their first-year photometry (Holtzman et al. 2008), spectroscopy (Zheng et al. 2008), and cosmological results (Kessler et al. 2009). Some of the first-year spectra (along with additional data) are also presented by Foley et al. (2010) and Konishi et al. (2011). Details of the SN photometry and spectral reductions can be found in those references. Details of the SN detection and selection for spectroscopic follow-up observations can be found in Sako et al. (2008). Here, we use the Zheng et al. (2008) compilation, which has 181 spectra of 131 SNe Ia.

The sample was culled using the same criteria outlined for the SNLS sample. Requiring photometric measurements reduced the sample to 99 spectra of 92 SNe Ia. Our light-curve shape and phase cut further reduced the sample to 47 spectra of 39 SNe Ia and 53 spectra of 44 SNe Ia for  $v_{\text{Ca H\&K}}^0$  and  $v_{\text{Si II}}^0$ , respectively. The quality of the spectra varies significantly across the sample, but there are many excellent spectra. After making the spectroscopy quality cuts above, we are left with a final SDSS sample of 19 spectra of 16 SNe Ia and 33 spectra of 27 SNe Ia for  $v_{\text{Ca H\&K}}^0$  and  $v_{\text{Si II}}^0$ , respectively. A summary of the cuts and how they affect the sample are presented in Table 1.

## 2.3. Combined High-Redshift Sample

Combining the SDSS-II and SNLS samples, we generate our high-redshift sample. This sample consists of 58 spectra with good  $v_{\text{Ca H\&K}}^0$  measurements for 54 SNe Ia with appropriate light-curve parameters. There are also 46 spectra with good  $v_{\text{Si II}}^0$  measurements for 40 SNe Ia with appropriate light-curve parameters in our high-redshift sample. There are a total of 75 high-redshift SNe Ia with at least one of the two ejecta velocities measured.

We present distributions of the stretch, SiFTO  $C$  (Conley et al. 2008), redshift, and host-galaxy mass for the full high-redshift, light-curve shape-cut high-redshift,  $v_{\text{Si II}}^0$  high-redshift, and  $v_{\text{Ca H\&K}}^0$  high-redshift samples in Figure 1. In that figure, the  $v_{\text{Si II}}^0$  high-redshift and  $v_{\text{Ca H\&K}}^0$  high-redshift samples were scaled such that the peaks of their histograms match the peaks of the light-curve shape-cut high-redshift sample histograms. Comparing the subsamples using Kolmogorov-Smirnov (K-S) tests shows that the subsamples with velocity information are mostly consistent with being drawn from the same parent population as the light-curve shape-cut high-redshift sample (all have  $p$ -values  $> 0.1$ ). The single exception is the  $v_{\text{Si II}}^0$  sample in regard to redshift, which has a K-S  $p$  value of  $7 \times 10^{-11}$ . The results of the K-S tests are similar when comparing the velocity subsamples to the full SNLS+SDSS sample except the stretch distributions are significantly different ( $p < 1 \times 10^{-5}$ ). Therefore, the velocity subsamples appear to be reasonable representations of the light-curve shape-cut high-redshift sample.

TABLE 1  
HIGH-REDSHIFT SPECTROSCOPY SAMPLE QUALITY CUTS

Cut / Sample	Full $v_{\text{Ca H\&K}}^0$	Full $v_{\text{Si II}}^0$	SDSS $v_{\text{Ca H\&K}}^0$	SDSS $v_{\text{Si II}}^0$	SNLS $v_{\text{Ca H\&K}}^0$	SNLS $v_{\text{Si II}}^0$
Full SDSS+SNLS Sample	511 (447)		181 (131)		330 (316)	
Has Photometric Measurements	311 (282)		99 (92)		212 (205)	
Light-Curve Shape and Phase	159 (145)	168 (154)	47 (39)	53 (44)	106 (101)	115 (110)
Spectrum Quality	58 (54)	46 (40)	19 (16)	33 (27)	39 (38)	13 (13)

NOTE. — Number of spectra and SNe are presented without and with parentheses, respectively.

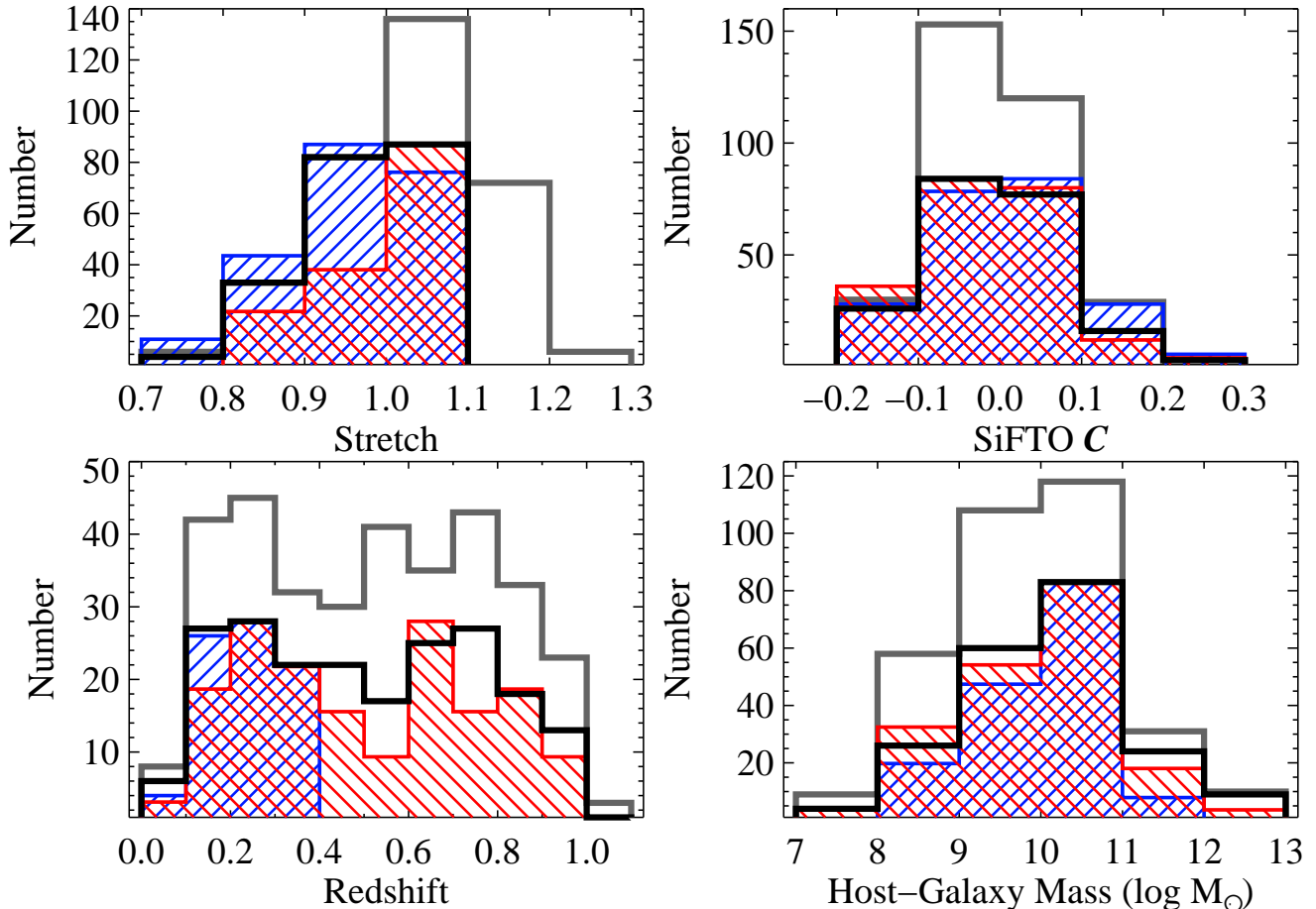


FIG. 1.— Histograms of stretch (upper left), SiFTO  $C$  (upper right), redshift (lower left), and host-galaxy mass (lower right) for the high-redshift sample. The full and light-curve shape-cut SDSS+SNLS samples are represented by the grey and black histograms, respectively. The  $v_{\text{Si II}}^0$  and  $v_{\text{Ca H\&K}}^0$  high-redshift samples are represented by the blue and red histograms, respectively; their histograms have been scaled such that their peaks match the peak of the light-curve shape-cut high-redshift histogram.

A table of all high-redshift SNe/spectra which pass our cuts, their light-curve measurements, and their ejecta velocity measurements can be found in Table 2.

#### 2.4. FSK11

FSK11 presented photometric and spectroscopic properties for a large sample of low-redshift SNe Ia. The spectroscopic sample was largely taken from the CfA Supernova Program (Matheson et al. 2008; S. Blondin et al., in preparation). The photometry was taken from the CfA3 (Hicken et al. 2009a) and LOSS (Ganeshalingam et al. 2011) samples. In total, the sample relies on 1630 optical spectra of 255 SNe Ia. The final sample consists of 42 and 65 SNe Ia which passed all quality cuts and have

measurements for  $v_{\text{Ca H\&K}}^0$  and  $v_{\text{Si II}}^0$ , respectively.

#### 3. EJECTA VELOCITY

Using the method of Blondin et al. (2006), we measure  $v_{\text{Si II}}$  and  $v_{\text{Ca H\&K}}$  for the high-redshift sample. Briefly, the spectra are deredshifted and smoothed using an inverse-variance-weighted Gaussian filter. The smoothed spectra are resampled on a fine wavelength scale with wavelength bins of 0.1 Å. The minimum of each feature (corresponding to the wavelength of maximum absorption) is recorded, and a velocity is measured using the relativistic Doppler formula. The uncertainty in the velocity measurements include the uncertainty of determining the wavelength of maximum absorption, dif-

ferences for assuming different smoothing scales, and redshift uncertainties. We exclude spectra that are of low quality and  $v_{\text{Ca H\&K}}$  measurements according to the criteria of FSK11 and outlined above.

The velocity inferred from the minimum of a spectral feature does not necessarily correspond to the “photospheric” velocity of the ejecta. If the line is saturated, the velocity measured from that line will be higher than that of the photospheric velocity. However, if the density profiles of the element responsible for the the spectral line is smooth with radius, the velocity inferred from the line is physically meaningful and a good proxy for the overall ejecta kinematics. The Ca H&K and Si II  $\lambda 6355$  features both have smooth velocity evolution with time for most SNe over the phase range we use in this study (FSK11), and therefore,  $v_{\text{Si II}}$  and  $v_{\text{Ca H\&K}}$  are good proxies for the overall ejecta velocity.

High-redshift SN Ia spectra tend to have much more galaxy contamination than those from SNe Ia at low redshift (Foley et al. 2008). High-redshift SN Ia spectra also tend to have a lower signal-to-noise ratio (S/N). We examined the possibility of lower S/N and higher galaxy-contamination biasing velocity measurements. Performing a Monte Carlo simulation which added various amounts of noise and galaxy contamination (from several different galaxy templates) to several SN Ia spectra found that there is a slight bias of  $\sim 200 \text{ km s}^{-1}$  to lower velocities with extreme galaxy contamination and relatively low S/N. Visual inspection of the spectra in the high-redshift sample that pass all of our cuts indicates that none have significant galaxy contamination, and thus any bias should be significantly less than our overall measurement uncertainty.

The SNLS has performed several spectroscopic studies, but only one, Bronder et al. (2008), provided ejecta velocity measurements. Bronder et al. (2008) only measure  $v_{\text{Ca H\&K}}$ , but did so by fitting a Gaussian to a 60-Å smoothed spectrum. This method is different from our method, and can provide significantly different velocity measurements if there are multiple components to the Ca H&K feature. Figure 2 compares the velocity measured by Bronder et al. (2008) to our measured velocity. The grey symbols are for all spectra with measurements in both samples, while the black symbols are for the spectra which pass all of our cuts. There is general agreement between the two studies; however for the spectra that do not pass all of our cuts, the Bronder et al. (2008) measurements span a smaller velocity range for the full sample. This is likely the result of the Gaussian fitting, which will tend to find an intermediate velocity if there are two velocity components. Our quality cuts typically reject such spectra (even if it provides a more accurate measurement of the velocity). All spectra which pass our quality cuts have consistent velocity measurements from both studies.

The SDSS-II survey also has several spectroscopic studies, but none present tabulated line velocities for a direct comparison.

As a SN photosphere recedes in velocity space with time, the ejecta velocity as measured from spectral features also decreases. Since spectra are obtained at various phases, a correction for this temporal evolution must be made to properly compare different SNe. FSK11

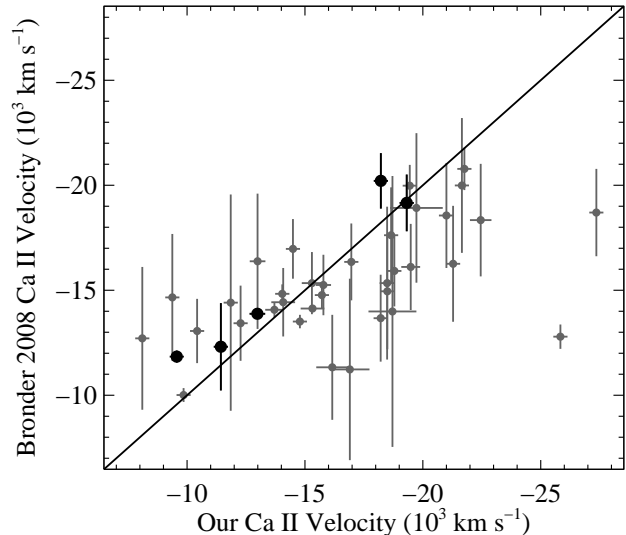


FIG. 2.—  $v_{\text{Ca H\&K}}$  measurements from Bronder et al. (2008) compared to the measurements presented here. The grey symbols are for all spectra for which a velocity was measured for both studies, including those that do not pass our quality cuts. The black symbols are for the 5 spectra from Bronder et al. (2008) that pass all of our cuts.

provides a prescription for making this correction. Using the time of maximum brightness measured from the light curves, along with the measurements of  $v_{\text{Si II}}$  and  $v_{\text{Ca H\&K}}$ , the high-redshift ejecta velocities are corrected to maximum brightness —  $v_{\text{Si II}}^0$  and  $v_{\text{Ca H\&K}}^0$  — using Equations 5 and 7 of FSK11. Uncertainties for these measurements include both the velocity uncertainties and the scatter in the relations. These measurements are provided in Table 2.

There are a handful of SNe with multiple spectra which pass our phase and quality cuts. Each of these spectra provide an independent measurement of the maximum-brightness ejecta velocity. In these cases, we choose the higher-quality spectrum to provide the adopted measurement. In cases where the difference in quality is not obvious, we choose the spectrum closer to maximum brightness, as was done by FSK11.

A table of all high-redshift SNe/spectra, light-curve measurements, and ejecta velocity measurements can be found in Table 2.

All measurements for the FSK11 sample are presented there.

## 4. RESULTS

### 4.1. Velocity Distributions

The FK11 relation between ejecta velocity and light-curve shape has significant implications for SN Ia cosmology. First, measuring ejecta velocity should improve the precision and accuracy of SN Ia distance measurements. However, since cosmological measurements are made from differential SN Ia distances, ignoring this effect biases cosmological results if either the low and high-redshift samples have different velocity distributions (and thus different intrinsic color distributions), or if the relation evolves with redshift.

If the intrinsic color distributions are different such

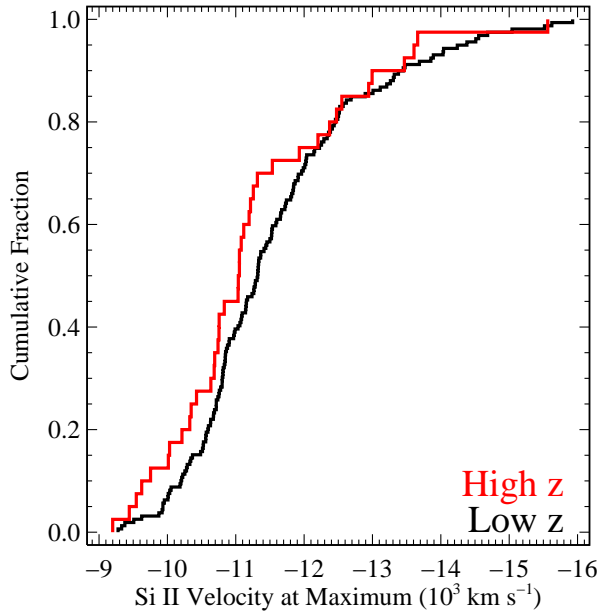


FIG. 3.—  $v_{\text{Si II}}^0$  CDF for the FSK11 (black) and high-redshift (red) samples.

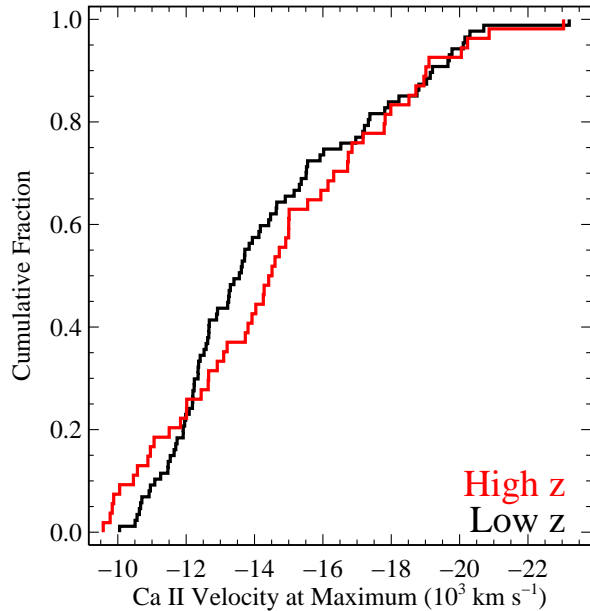


FIG. 4.—  $v_{\text{Ca H\&K}}^0$  CDF for the FSK11 (black) and high-redshift (red) samples.

that the average intrinsic color is different for low and high redshift, then the differential extinction correction will be incorrect. To test this possibility, we compare the velocity distributions of the FSK11 and high-redshift samples. The FSK11 sample may not completely overlap with the Conley et al. (2011) low-redshift cosmology sample, but it is representative of the observed low-redshift population. Similarly, the culled high-redshift sample presented here should be representative of the full high-redshift sample (with the same light-curve parameters). To mitigate any possible correlation between highly reddened SNe Ia (which are not found at high redshift) and velocity, we remove all SNe Ia with  $B_{\text{max}} - V_{\text{max}} > 0.4$  mag from the FSK11 sample.

Figures 3 and 4 present the  $v_{\text{Si II}}^0$  and  $v_{\text{Ca H\&K}}^0$  cumulative distribution functions (CDFs), respectively, for the FSK11 and high-redshift samples. The two samples appear relatively similar for both quantities. K-S tests result in  $p$ -values of 0.10 and 0.20 for  $v_{\text{Si II}}^0$  and  $v_{\text{Ca H\&K}}^0$ , respectively. From these tests, there is no indication that the samples are pulled from different parent populations in regard to ejecta velocity.

There is no significant velocity offset between the low and high-redshift samples. As will be shown in Section 4.2, ejecta velocity and intrinsic color are correlated for our high-redshift sample. Assuming that the relations between ejecta velocity and intrinsic color are the same at low and high redshift and since the low and high-redshift samples have similar ejecta velocity distributions, it is unlikely that the low and high-redshift samples have significantly different intrinsic colors. Therefore, it is unlikely that cosmological measurements are highly biased by not accounting for the velocity-color relation. However, the high-redshift samples are still small, and even a small offset could affect cosmological measurements. Future surveys and studies should consider the possibility of a difference in low and high-redshift SN Ia ejecta

velocities.

#### 4.2. Correlation Between Ejecta Velocity and Color

FK11 showed that SNe Ia with high ejecta velocity (as determined by Si II  $\lambda 6355$ ) have redder intrinsic  $B_{\text{max}} - V_{\text{max}}$  colors than SNe Ia with low ejecta velocity. FSK11 showed this relation held when using Ca H&K to determine ejecta velocity and further showed that a linear function adequately describes the relation between intrinsic  $B_{\text{max}} - V_{\text{max}}$  ( $(B_{\text{max}} - V_{\text{max}})_0$ ) and  $v_{\text{Si II}}^0$ . Here, we test the relation between ejecta velocity and intrinsic color for the high-redshift sample. If this relation evolves with redshift, cosmological measurements can be significantly affected.

Unfortunately, there are no published measurements of  $B_{\text{max}} - V_{\text{max}}$  for the high-redshift sample. However, there are measurements of  $\mathcal{C}$ , the color parameter from SiFTO (Conley et al. 2008). SiFTO does not attempt to distinguish intrinsic color and dust extinction, and parameterizes differences in apparent color as a single parameter,  $\mathcal{C}$ . Examining this parameter is similar to examining an observed  $B_{\text{max}} - V_{\text{max}}$ . The high-redshift sample consists of SNe Ia with little to no dust reddening. Therefore, using  $\mathcal{C}$  as a proxy for intrinsic color is a reasonable first approximation.

Figure 5 presents  $v_{\text{Ca H\&K}}^0$  as a function of  $\mathcal{C}$  for the high-redshift sample. Performing a Bayesian Monte-Carlo linear regression on the data (Kelly 2007) with  $2 \times 10^6$  realizations, we find that 99.995% of the realizations have a negative slope (all but 11), which corresponds to a 4.0- $\sigma$  result. The linear correlation coefficient is  $-0.61$ . There is a strong relation between ejecta velocity and observed color for the high-redshift sample, with the higher-velocity SNe Ia having redder colors. This is similar to what was found for the low-redshift sample (Pignata et al. 2008; Wang et al. 2009).

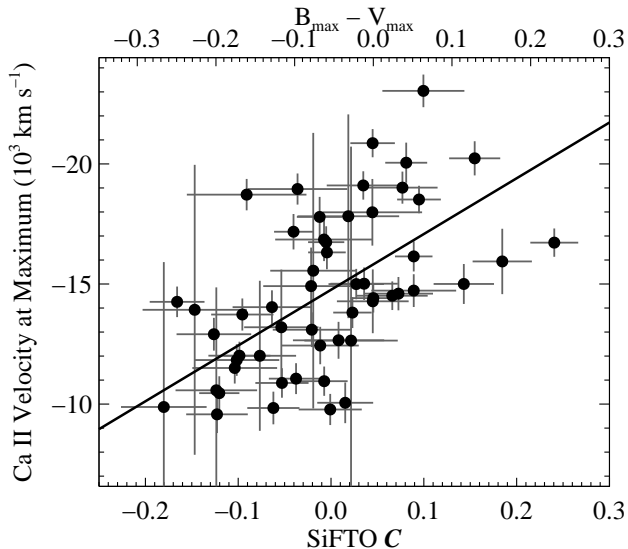


FIG. 5.— Maximum-light Ca II H&K velocity ( $v_{\text{Ca H\&K}}$ ) as a function of SiFTO  $\mathcal{C}$ . The equivalent values for  $B_{\text{max}} - V_{\text{max}}$  as determined by Equation 1 are presented on the top axis. The solid line represents the best-fit linear model for the data.

Performing the same analysis with  $v_{\text{Si II}}^0$ , we find a worse linear correlation coefficient of  $-0.28$  and the linear trend is less than a  $2\text{-}\sigma$  result. This difference may be the result of the small sample or possibly the relatively small number of SNe Ia with high-velocity Si II  $\lambda 6355$  (11/40 SNe Ia with a  $v_{\text{Si II}}^0$  measurement have velocities above  $-11,800 \text{ km s}^{-1}$ ), preventing a strong linear trend. Future larger samples will determine if the low-significance trend seen with  $v_{\text{Si II}}^0$  and  $\mathcal{C}$  is real at high redshift.

As mentioned above,  $\mathcal{C}$  is a reasonable proxy for the observed SN color. Using the intersection of the low-redshift sample used by Conley et al. (2011) and the FSK11 sample, we are able to determine a relation between  $\mathcal{C}$  and  $B_{\text{max}} - V_{\text{max}}$ . The measurements for the 41 SNe Ia in both samples with our adopted  $\Delta m_{15}(B)$  range are presented in Figure 6. The two quantities are highly correlated and a linear fit to the data provides the following relation:

$$B_{\text{max}} - V_{\text{max}} = (1.18 \pm 0.11)\mathcal{C} - (0.054 \pm 0.008). \quad (1)$$

If one uses all 65 SNe Ia in the matched sample, the relation is statistically equivalent. Since the two quantities are highly correlated,  $v_{\text{Ca H\&K}}^0$  is also highly correlated with  $B_{\text{max}} - V_{\text{max}}$  for the high-redshift sample.

Using the measurement of the observed rest-frame  $B$ -band maximum brightness,  $m_B$ , along with the measured stretch and a distance modulus,  $\mu$ , we can determine the light-curve shape corrected peak absolute  $B$  magnitude,  $M'_B$ . The choice of cosmological parameters for determining the distance modulus will slightly change the value of  $M'_B$ . We choose to use the best-fit Sullivan et al. (2011) Flat  $w$ CDM values of  $(\alpha, \Omega_m, w) = (1.451, 0.269, -1.061)$ . We also use  $H_0 = 70.5 \text{ km s}^{-1} \text{ Mpc}^{-1}$  to match the analyses of FK11 and FSK11, but the choice of  $H_0$  only affects the overall normalization. Choosing a Flat  $\Lambda$ CDM cosmology with  $\Omega_m = 0.3$  makes little difference on the results of our analysis. We further adjust the absolute magnitude to account for the corre-

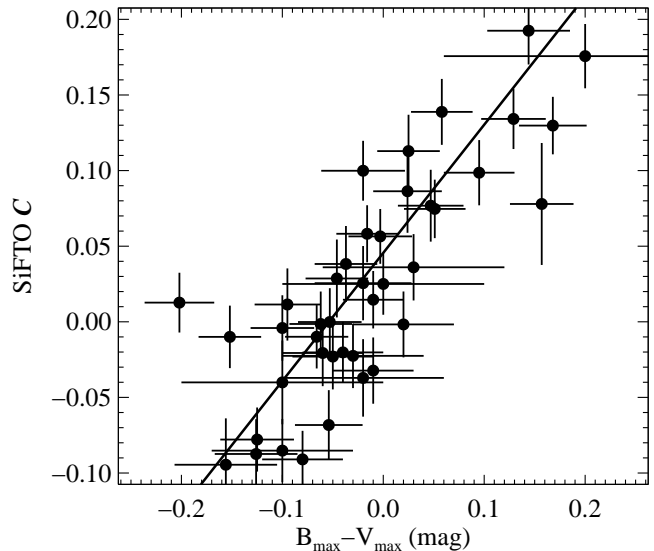


FIG. 6.—  $B_{\text{max}} - V_{\text{max}}$  and SiFTO  $\mathcal{C}$  measurements for the 41 low-redshift SNe Ia with measurements from Conley et al. (2011) and FSK11 and with  $0.9 \leq \Delta m_{15}(B) \leq 1.5$  mag. The line represents the best linear fit to the data.

lation between Hubble residuals and host-galaxy mass (Kelly et al. 2010; Lampeitl et al. 2010; Sullivan et al. 2010). SNe Ia hosted in high mass galaxies ( $M > 10^{10} M_{\odot}$ ) tend to be brighter by  $0.05 - 0.1$  mag after correction for both stretch and  $\mathcal{C}$ . We use the magnitude difference of Sullivan et al. 2011 of  $\Delta M = 0.076$  mag to further correct  $M_B$ . Specifically,  $M_B = M'_B$  and  $M_B = M'_B + \Delta M$  for SNe Ia hosted in galaxies with  $M \leq 10^{10}$  and  $M > 10^{10} M_{\odot}$ , respectively. We have performed our analysis both with and without this correction, and it makes only a slight difference in the significance of our results.

Figures 7 and 8 present  $M_B$  as a function of  $B_{\text{max}} - V_{\text{max}}$  for the high-redshift sample. These figures are similar to Figure 19 from FSK11. The symbols are color-coded by  $v_{\text{Ca H\&K}}^0$  and  $v_{\text{Si II}}^0$  for Figures 7 and 8, respectively. There is a general trend that redder SNe are also fainter. Since we have already corrected for light-curve shape, this is presumably the result of dust reddening. We overplot the reddening law found by Foley & Kasen (2011) for the low-velocity sample<sup>4</sup>, which matches the general trend mentioned above. This reddening law is extremely similar to the color-correction trend  $\beta\mathcal{C}$  used by SiFTO assuming the best-fit value for  $\beta$  from Sullivan et al. (2011). We have performed our analysis using both relations, and our results do not change if we choose a particular relation.

As was done by FSK11, we use the color offset from the dust reddening line to determine the intrinsic  $B_{\text{max}} - V_{\text{max}}$  pseudo-color. Figures 9 and 10 display  $v_{\text{Ca H\&K}}^0$  and  $v_{\text{Si II}}^0$  as a function of intrinsic  $B_{\text{max}} - V_{\text{max}}$  for the high-redshift sample. As was seen in the low-redshift sample (FK11; FSK11), SNe Ia with higher-velocity ejecta tend to be intrinsically redder. The color and veloc-

<sup>4</sup> The reddening law was slightly adjusted to account for the high-redshift data using  $M_B$ , while the low-redshift samples used  $M_V$ . This required accounting for  $R_B = R_V + 1$  and a slight offset in the magnitude of zero color.

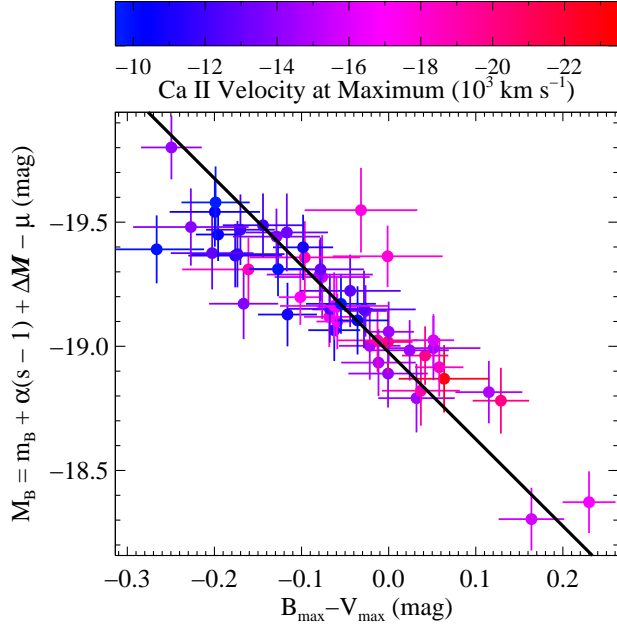


FIG. 7.— The light-curve shape and host-mass corrected peak absolute  $B$  brightness as a function of  $B_{\max} - V_{\max}$ . The color of the symbol corresponds to the SN’s  $v_{\text{Ca H\&K}}^0$ , with the color bar at the top of the figure displaying the correspondence. The solid black line represents the host-galaxy dust reddening of a zero-color SN Ia. The deviations from this line in color is the intrinsic color of a given SN.

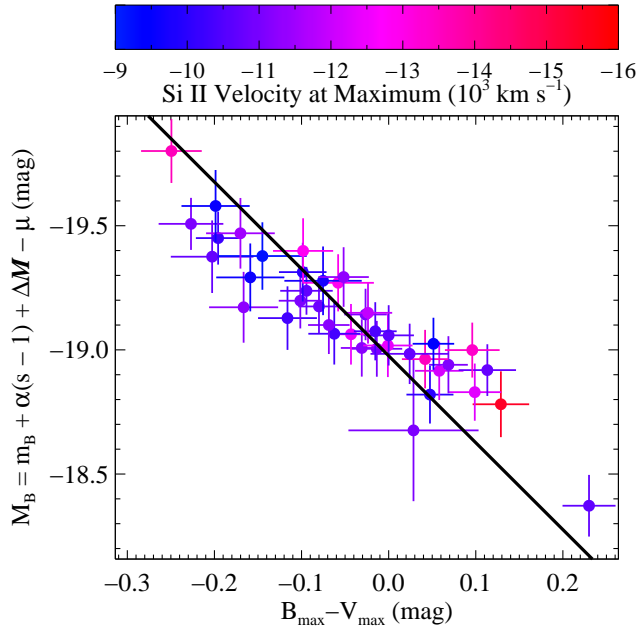


FIG. 8.— Same as Figure 7, except for the high-redshift sample with  $v_{\text{Si II}}^0$  measurements and with the symbols color-coded by  $v_{\text{Si II}}^0$ .

ity have a linear correlation coefficients of  $-0.71$  and  $-0.53$  for  $v_{\text{Ca H\&K}}^0$  and  $v_{\text{Si II}}^0$ , respectively, indicating good correlations. The correlation between  $v_{\text{Ca H\&K}}^0$  and intrinsic color is much better for the high-redshift sam-

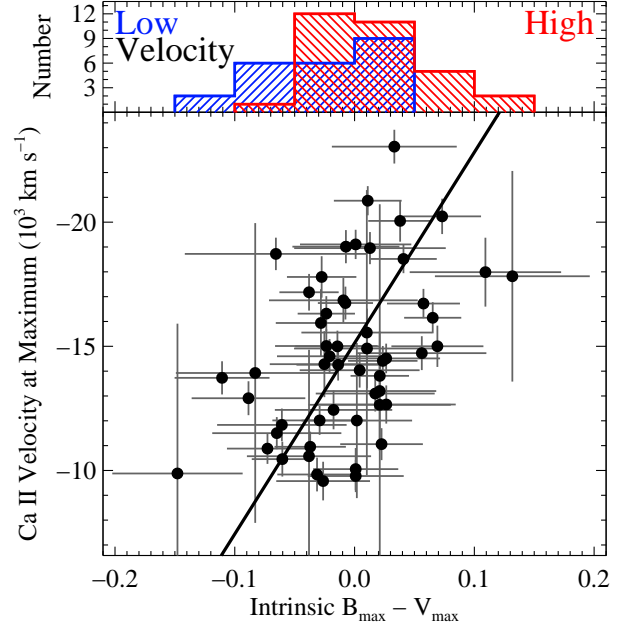


FIG. 9.— Maximum-light Ca II H&K velocity ( $v_{\text{Ca H\&K}}^0$ ) as a function of intrinsic  $B_{\max} - V_{\max}$  pseudo-color for the high-redshift sample of SNe Ia. The solid line is the best-fit linear model for the data. The histograms (top panel) show the intrinsic  $B_{\max} - V_{\max}$  pseudo-color distribution for subsamples split by  $v_{\text{Ca H\&K}}^0 = -14,000$  km s $^{-1}$ , with the blue and red histograms representing the low and high-velocity subsamples, respectively.

ple than what was found for the low-redshift sample ( $\rho = -0.24$ ; FSK11), but similar for  $v_{\text{Si II}}^0$ . Performing a Bayesian Monte-Carlo linear regression on the  $v_{\text{Ca H\&K}}^0$  data (Kelly 2007), we find that 99.8% of the realizations have a negative slope, corresponding to a  $3.1\text{-}\sigma$  result. The best-fit relation is

$$(B_{\max} - V_{\max})_0 = (-0.20 \pm 0.06) - (0.013 \pm 0.004) \times (v_{\text{Ca H\&K}}^0 / 1000 \text{ km s}^{-1}) \text{ mag.} \quad (2)$$

It is somewhat surprising that the trend is statistically significant since a linear trend was not significant for the low-redshift sample (FSK11).

Performing the same analysis for  $v_{\text{Si II}}^0$ , we find that 98.8% of the Monte Carlo realizations have a negative slope, corresponding to only a  $2.5\text{-}\sigma$  result. Although this does not qualify as a statistically significant result, the best-fit line is similar to that of the low-redshift sample. The relatively small number of high-velocity events (11/40 SNe Ia with a  $v_{\text{Si II}}^0$  measurement have velocities above  $-11,800$  km s $^{-1}$ ) likely contributes to the low significance. Additional high-redshift data should be able to determine if the linear relation is real.

Along with the linear analysis, we examine the  $v_{\text{Ca H\&K}}^0$  and  $v_{\text{Si II}}^0$  samples after splitting them into low and high-velocity (using  $-14,000$  and  $-11,800$  km s $^{-1}$  for  $v_{\text{Ca H\&K}}^0$  and  $v_{\text{Si II}}^0$ , respectively). As shown by the histograms in Figures 9 and 10, the low and high-velocity subsamples are offset in intrinsic color. The low/high-velocity subsamples have mean  $(B_{\max} - V_{\max})_0$  pseudo-colors of  $-0.028 \pm 0.008 / 0.013 \pm 0.006$  and  $-0.005 \pm 0.006 / 0.030 \pm 0.009$  mag for the  $v_{\text{Ca H\&K}}^0$  and  $v_{\text{Si II}}^0$  samples,



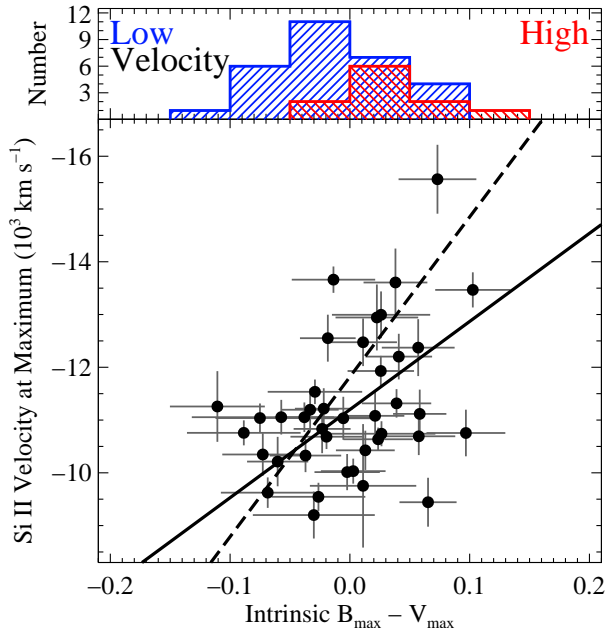


FIG. 10.— Maximum-light Si II  $\lambda 6355$  velocity ( $v_{\text{Si II}}^0$ ) as a function of intrinsic  $B_{\text{max}} - V_{\text{max}}$  pseudo-color for the high-redshift sample of SNe Ia. The solid line is the best-fit linear model for the data. The dashed line is the linear relation found for the low-redshift sample (FSK11). The histograms (top panel) show the intrinsic  $B_{\text{max}} - V_{\text{max}}$  pseudo-color distribution for subsamples split by  $v_{\text{Si II}}^0 = -11,800 \text{ km s}^{-1}$ , with the blue and red histograms representing the low and high-velocity subsamples, respectively.

respectively. For both measurements of the ejecta velocity, there is an  $\sim 0.04$  mag offset between the low and high-velocity average intrinsic colors that is significant at the  $3.3 / 4.5\text{-}\sigma$  level. However, any linear relation between  $B_{\text{max}} - V_{\text{max}}$  and  $v_{\text{Ca H\&K}}^0$  should underestimate the statistical difference by simply separating the sample into two velocity groups.

Finally, we perform K-S tests on the low and high-velocity subsamples. When comparing the velocity subsamples, the K-S  $p$ -values for the  $v_{\text{Ca H\&K}}^0$  and  $v_{\text{Si II}}^0$  samples are  $5.0 \times 10^{-3}$  and  $8.9 \times 10^{-3}$ , respectively. The K-S tests therefore indicate that the low and high-velocity subsamples are drawn from different parent populations in regard to intrinsic color.

An offset of 0.04 mag in  $B_{\text{max}} - V_{\text{max}}$ , the difference in the median values for the low and high-velocity subsamples, corresponds to a difference in  $A_V$  of 0.08 to 0.12 mag for  $2 \leq R_V \leq 3.1$ . The high-redshift sample has an intrinsic color dispersion,  $\sigma_{(B_{\text{max}} - V_{\text{max}})_0}$ , of 0.051 and 0.050 mag for  $v_{\text{Ca H\&K}}^0$  and  $v_{\text{Si II}}^0$ , respectively, but splitting the sample by velocity results in  $\sigma_{(B_{\text{max}} - V_{\text{max}})_0} = 0.048$  (0.050) and 0.044 (0.036) mag for the low and high-velocity  $v_{\text{Ca H\&K}}^0$  ( $v_{\text{Si II}}^0$ ) subsamples, respectively. This is similar to what was found for the FSK11 sample; however, unlike the FSK11 sample, the low-velocity high-redshift sample does not have a significantly smaller color scatter than the high-velocity sample.

#### 4.3. Ejecta Velocity and Host-Galaxy Mass

It has long been known that SNe Ia in different hosts have different peak luminosities (e.g., Branch et al. 1996; Hamuy et al. 1996; Howell 2001). The observed correlation between SN Ia host-galaxy mass, morphology, and star-formation rate and Hubble residuals (Hicken et al. 2009b; Kelly et al. 2010; Lampeitl et al. 2010; Sullivan et al. 2010) improves SN Ia distance measurements and points to a possible connection between SN Ia progenitor properties and SN luminosity that are not already removed by accounting for light-curve shape. The secondary effect is such that SNe Ia hosted in galaxies with  $M \geq 10^{10} M_{\odot}$  are 0.05 – 0.1 mag brighter than those with the same light-curve properties hosted in less massive galaxies after making initial corrections. Since the intrinsic color difference between low and high-velocity SNe Ia can cause an incorrect distance measurement, and thus absolute magnitude measurement, of the same order of magnitude, it is prudent to determine if SN Ia ejecta velocity is correlated with host-galaxy mass.

The correlation between ejecta velocity and host-galaxy mass has not been investigated at any redshift. To increase our sample, we combine the high-redshift sample with the low-redshift FSK11 sample matched to the Conley et al. (2011) sample to provide consistent host-galaxy mass measurements. This increases our sample by 14 and 23 SNe Ia for our  $v_{\text{Ca H\&K}}^0$  and  $v_{\text{Si II}}^0$  samples. Several SNe Ia have reported host-galaxy masses equal to the maximum mass in the Conley et al. (2011) sample. These SNe either had no host-galaxy photometry available to the SNLS team or saturated the galaxy model at the high-mass end. Since most were low-redshift SNe, they were assigned to the high-mass bin and the probability that they were low mass was taken as a systematic uncertainty (A. Conley, private communication). The lack of an accurate mass estimate for these galaxies reduces their usefulness for our study, and we therefore exclude these SNe from our analysis. In the total combined sample, there are 67 and 63 SNe Ia with  $v_{\text{Ca H\&K}}^0$  and  $v_{\text{Si II}}^0$  measurements, respectively.

Comparing  $v_{\text{Ca H\&K}}^0$  to host-galaxy mass, there is a reasonable linear correlation ( $\rho = 0.31$ ), and a Bayesian Monte-Carlo linear regression results in 98.4% of the realizations having a positive slope (a  $2.4\text{-}\sigma$  result). Figure 11 displays  $v_{\text{Ca H\&K}}^0$  as a function of host-galaxy mass. There is a slight visible trend such that more massive galaxies tend to host SNe Ia with lower  $v_{\text{Ca H\&K}}^0$ . It also appears that SNe Ia in high-mass galaxies have a larger spread in  $v_{\text{Ca H\&K}}^0$ .

One worry is that the relations between host-galaxy mass, stretch, and intrinsic color may cause the observed relation. Similar to what was found by FSK11, there is no correlation between light-curve shape and either ejecta velocity or intrinsic color for the high-redshift sample ( $\rho = -0.066$  for stretch and  $v_{\text{Ca H\&K}}^0$ ;  $\rho = -0.070$  for stretch and  $(B_{\text{max}} - V_{\text{max}})_0$ ). The correlation between stretch and  $v_{\text{Ca H\&K}}^0$  is slightly larger for the combined low and high redshift sample ( $\rho = -0.111$ ), but still not significant. The correlation between host-galaxy mass and stretch does not appear to be causing the correlation between host-galaxy mass and intrinsic color for our sample.

There is no significant linear relation between host-galaxy mass and  $v_{\text{Ca H\&K}}^0$  for our sample, but the signif-

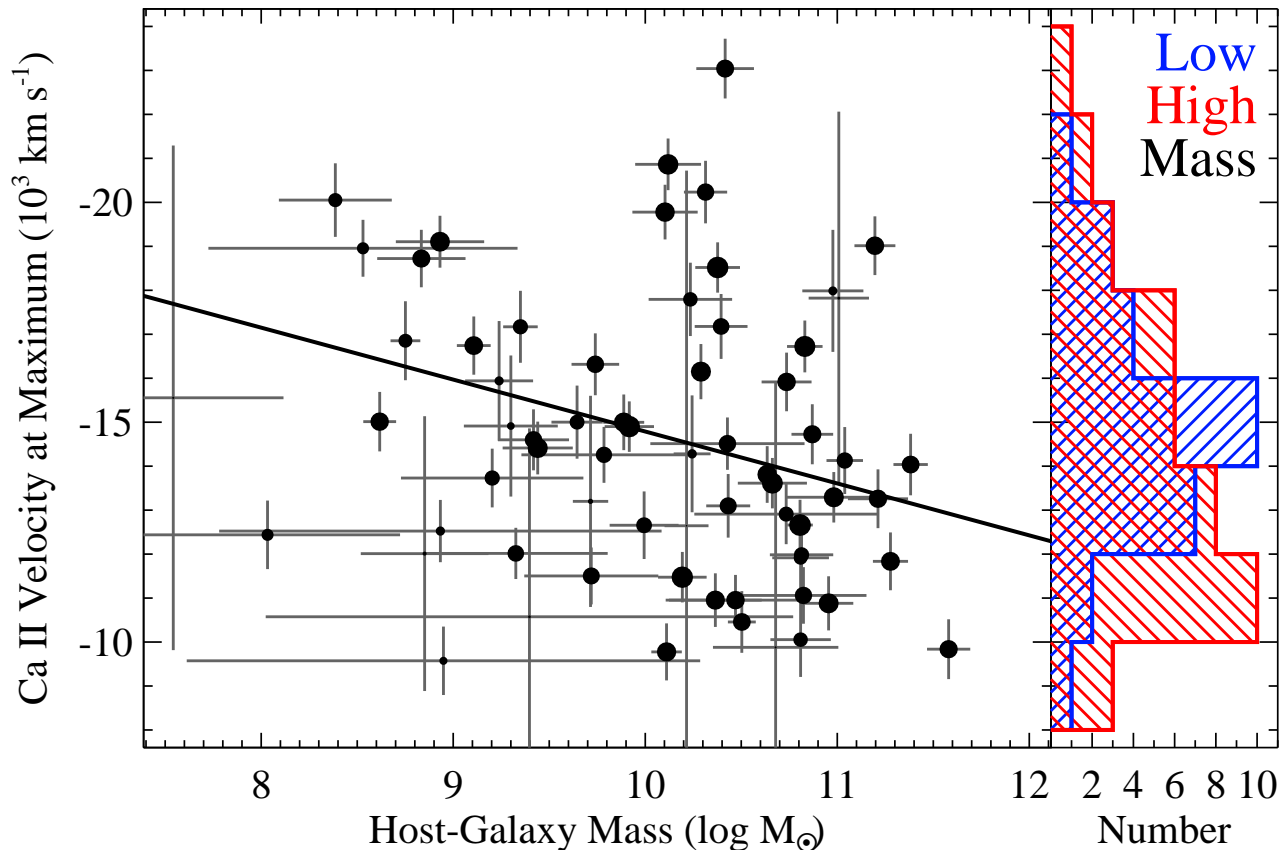


FIG. 11.— Left panel:  $v_{\text{Ca H\&K}}^0$  for the  $v_{\text{Ca H\&K}}^0$  high-redshift sample of SNe Ia as a function of host-galaxy mass. The size of the symbols is inversely proportional to the size of the uncertainties. The best-fit linear model to the data is shown as a solid line. Right panel:  $v_{\text{Ca H\&K}}^0$  histograms for the high-redshift SNe Ia hosted in galaxies with masses above/below  $10^{10} M_{\odot}$  (red/blue histograms).

inance level warrants a further investigation with larger data sets. Splitting the sample at  $10^{10} M_{\odot}$ , the low and high-mass samples have average  $v_{\text{Ca H\&K}}^0$  of  $-15,050 \pm 140$  and  $-14,370 \pm 110 \text{ km s}^{-1}$ , respectively. Using Equation 2, the velocity offset corresponds to an intrinsic color offset of 0.009 mag. If this is incorrectly attributed to dust, it would correspond to an error in a distance estimate of 0.018 to 0.027 mag for  $2 \leq R_V \leq 3.1$ .

There is no significant relation between  $v_{\text{Si II}}^0$  and host-galaxy mass for our sample. Since  $v_{\text{Ca H\&K}}^0$  is strongly correlated with intrinsic color and potentially correlated with host-galaxy mass, one might expect that intrinsic color and host-galaxy mass are correlated. We performed this analysis on the full Conley et al. (2011) sample and find no significant correlation.

## 5. DISCUSSION & CONCLUSIONS

Using the high-redshift sample, we identified 40 and 54 high-redshift SNe Ia with appropriate light-curve shapes, spectral phases, and spectral data quality to measure the maximum-light Ca H&K and Si II  $\lambda 6355$  ejecta velocities ( $v_{\text{Ca H\&K}}^0$  and  $v_{\text{Si II}}^0$ ), respectively. We compare the distributions of ejecta velocity for the high-redshift sample to the distributions of the low-redshift FSK11 sample, finding no statistically significant difference in the distributions for the two samples. We measure the intrinsic  $B_{\text{max}} - V_{\text{max}}$  pseudo-color for the high-redshift sample. The ejecta velocity is highly correlated with

$(B_{\text{max}} - V_{\text{max}})_0$ , such that SNe Ia with higher ejecta velocity tend to be redder. This is similar to what has been shown for the low-redshift sample (FK11; FSK11). We compare ejecta velocity to host-galaxy mass, finding a slight trend between the quantities such that SNe Ia hosted in lower-mass galaxies tend to have higher ejecta velocities than those hosted in higher-mass galaxies. The significance of this relation is still low, and future studies should examine this relation further.

A larger data set is required to determine if the average SN Ia ejecta velocity changes with redshift. This is particularly true for  $v_{\text{Si II}}^0$ , which is hampered by its relatively red wavelength. Near-infrared spectroscopy could increase the sample of SNe Ia with  $v_{\text{Si II}}^0$  measurements at high redshift.

The confirmation of the velocity-color relation at high redshift is an important step towards better cosmological measurements. Although the velocity-color relation affects some light-curve properties (Ganeshalingam et al. 2011; Cartier et al. 2011), it is still unclear if one can infer the ejecta velocity or intrinsic color of SNe Ia from their light curves alone. Therefore, the most precise SN Ia distance measurements at all redshifts continue to require spectroscopy.

The asymmetric explosion model suggests that the distribution of measured ejecta velocities can be explained by asymmetric explosions and viewing explosions from different viewing angles (Maeda et al. 2010;

Foley & Kasen 2011). If this model is correct, our measured distribution of ejecta velocities for low and high-redshift SNe Ia indicate that approximately the same amount of asymmetry is present at low and high redshifts, further indicating that SN Ia explosions do not evolve significantly from  $z = 0$  to  $z \approx 0.5$ . Regardless of symmetry, this result also indicates that the distribution of kinetic energy per unit mass is similar across this redshift range.

The tentative relation between ejecta velocity and host-galaxy mass may, if confirmed, provide insight into the relation between host-galaxy mass and Hubble residuals. Ejecta velocity is more directly connected to the SN properties than the host-galaxy mass, and might help the search for the physical driver of this relation.

Additional high-redshift data from SDSS-II and SNLS, which has already been obtained, will significantly in-

crease this sample. Current and future high-redshift SN surveys such as Pan-STARRS, the Dark Energy Survey, and eventually the Large Synoptic Survey Telescope, will provide large samples of high-redshift SNe Ia. However, spectroscopy from other telescopes is required to further examine the relations between ejecta velocity, intrinsic color, and host-galaxy properties at high redshift.

R.J.F. is supported by a Clay Fellowship.

This work was started and completed while R.J.F. was visiting the Carnegie Observatories in Pasadena. He thanks J. Simon, J. Kollmeier, and E. Teague for facilitating this extremely stimulating visit. He thanks N. Sanders for providing comments and A. Conley for helping determine the fidelity of some of the data.

#### REFERENCES

- Amanullah, R., et al. 2010, *ApJ*, 716, 712  
 Astier, P., et al. 2006, *A&A*, 447, 31  
 Baade, W. 1938, *ApJ*, 88, 285  
 Balland, C., et al. 2009, *A&A*, 507, 85  
 Blondin, S., et al. 2006, *AJ*, 131, 1648  
 Branch, D., Romanishin, W., & Baron, E. 1996, *ApJ*, 465, 73  
 Bronder, T. J., et al. 2008, *A&A*, 477, 717  
 Cartier, R., Forster, F., Coppi, P., Hamuy, M., Maeda, K., Pignata, G., Folatelli, G., & . 2011, *ArXiv e-prints*, 1110.0480  
 Coil, A. L., et al. 2000, *ApJ*, 544, L111  
 Conley, A., Carlberg, R. G., Guy, J., Howell, D. A., Jha, S., Riess, A. G., & Sullivan, M. 2007, *ApJ*, 664, L13  
 Conley, A., et al. 2011, *ApJS*, 192, 1  
 ——. 2008, *ApJ*, 681, 482  
 Ellis, R. S., et al. 2008, *ApJ*, 674, 51  
 Foley, R. J., et al. 2008, *ApJ*, 684, 68  
 ——. 2010, *ArXiv e-prints*, 1010.2749  
 Foley, R. J., & Kasen, D. 2011, *ApJ*, 729, 55  
 Foley, R. J., et al. 2009, *AJ*, 137, 3731  
 Foley, R. J., Sanders, N. E., & Kirshner, R. P. 2011, *ApJ*, 742, 89  
 Frieman, J. A., et al. 2008, *AJ*, 135, 338  
 Ganeshalingam, M., Li, W., & Filippenko, A. V. 2011, *MNRAS*, 416, 2607  
 Guy, J., et al. 2010, *A&A*, 523, A7+  
 Hamuy, M., Phillips, M. M., Suntzeff, N. B., Schommer, R. A., Maza, J., & Aviles, R. 1996, *AJ*, 112, 2391  
 Hicken, M., et al. 2009a, *ApJ*, 700, 331  
 Hicken, M., Wood-Vasey, W. M., Blondin, S., Challis, P., Jha, S., Kelly, P. L., Rest, A., & Kirshner, R. P. 2009b, *ApJ*, 700, 1097  
 Höflich, P., Wheeler, J. C., & Thielemann, F.-K. 1998, *ApJ*, 495, 617  
 Holtzman, J. A., et al. 2008, *AJ*, 136, 2306  
 Hook, I. M., et al. 2005, *AJ*, 130, 2788  
 Howell, D. A. 2001, *ApJ*, 554, L193  
 Howell, D. A., Sullivan, M., Conley, A., & Carlberg, R. 2007, *ApJ*, 667, L37  
 Howell, D. A., et al. 2006, *Nature*, 443, 308  
 ——. 2005, *ApJ*, 634, 1190  
 Kasen, D., & Plewa, T. 2007, *ApJ*, 662, 459  
 Kelly, B. C. 2007, *ApJ*, 665, 1489  
 Kelly, P. L., Hicken, M., Burke, D. L., Mandel, K. S., & Kirshner, R. P. 2010, *ApJ*, 715, 743  
 Kessler, R., et al. 2009, *ApJS*, 185, 32  
 Kirshner, R. P., et al. 1993, *ApJ*, 415, 589  
 Konishi, K., et al. 2011, *ArXiv e-prints*, 1101.1565  
 Kowal, C. T. 1968, *AJ*, 73, 1021  
 Lampeitl, H., et al. 2010, *ApJ*, 722, 566  
 Lentz, E. J., Baron, E., Branch, D., Hauschildt, P. H., & Nugent, P. E. 2000, *ApJ*, 530, 966  
 Leonard, D. C., Li, W., Filippenko, A. V., Foley, R. J., & Chornock, R. 2005, *ApJ*, 632, 450  
 Maeda, K., et al. 2010, *Nature*, 466, 82  
 ——. 2011, *MNRAS*, 413, 3075  
 Matheson, T., et al. 2005, *AJ*, 129, 2352  
 ——. 2008, *AJ*, 135, 1598  
 Maund, J. R., et al. 2010, *ApJ*, 725, L167  
 Mazzali, P. A., & Podsiadlowski, P. 2006, *MNRAS*, 369, L19  
 Miknaitis, G., et al. 2007, *ApJ*, 666, 674  
 Nugent, P., Baron, E., Branch, D., Fisher, A., & Hauschildt, P. H. 1997, *ApJ*, 485, 812  
 Östman, L., et al. 2011, *A&A*, 526, A28+  
 Perlmutter, S., et al. 1999, *ApJ*, 517, 565  
 Phillips, M. M. 1993, *ApJ*, 413, L105  
 Pignata, G., et al. 2008, *MNRAS*, 388, 971  
 Riess, A. G., et al. 1998, *AJ*, 116, 1009  
 Riess, A. G., Press, W. H., & Kirshner, R. P. 1996, *ApJ*, 473, 88  
 Riess, A. G., et al. 2007, *ApJ*, 659, 98  
 Röpke, F. K., & Hillebrandt, W. 2004, *A&A*, 420, L1  
 Sako, M., et al. 2008, *AJ*, 135, 348  
 Sauer, D. N., et al. 2008, *MNRAS*, 391, 1605  
 Sullivan, M., et al. 2010, *MNRAS*, 406, 782  
 ——. 2011, *ApJ*, 737, 102  
 Walker, E. S., et al. 2011, *MNRAS*, 410, 1262  
 Wang, X., et al. 2009, *ApJ*, 699, L139  
 Wood-Vasey, W. M., et al. 2007, *ApJ*, 666, 694  
 Zheng, C., et al. 2008, *AJ*, 135, 1766

TABLE 2  
 HIGH-REDSHIFT SPECTROSCOPY SAMPLE

SN	Redshift	Phase (days)	Stretch	SiFTO $C$	$m_B$ (mag)	Host Mass (log $M_\odot$ )	$v_{\text{Ca H\&K}}$ ( $10^3$ km s $^{-1}$ )	$v_{\text{Si II}}$ ( $10^3$ km s $^{-1}$ )	$v_{\text{Ca}^0}$ ( $10^3$ km s $^{-1}$ )
SDSS2165	0.2880 (0.0050)	6.19 (0.33)	1.06 (0.05)	-0.096 (0.034)	21.604 (0.043)	9.203 (0.475)	-13.28 (0.35)	-10.78 (0.63)	-13.70 (0.30)
SDSS2372	0.1810 (0.0005)	2.13 (0.20)	1.03 (0.03)	0.045 (0.024)	20.580 (0.035)	10.119 (0.171)	-19.93 (0.14)	-12.23 (0.39)	-20.80 (0.15)
SDSS2561	0.1180 (0.0002)	0.01 (0.15)	0.99 (0.02)	0.086 (0.023)	19.813 (0.033)	10.574 (0.086)	...	-10.03 (0.09)	...
SDSS2561 <sup>a</sup>	0.1180 (0.0002)	0.01 (0.15)	0.99 (0.02)	0.086 (0.023)	19.813 (0.033)	10.574 (0.086)	...	-9.10 (0.25)	...
SDSS2789	0.2900 (0.0005)	3.93 (0.33)	0.90 (0.05)	-0.077 (0.043)	21.576 (0.056)	10.949 (0.191)	...	-9.16 (0.39)	...
SDSS2916 <sup>a</sup>	0.1240 (0.0005)	-2.32 (0.14)	0.88 (0.03)	0.066 (0.038)	19.937 (0.062)	10.428 (0.401)	-15.08 (0.20)	-11.02 (0.19)	-14.70 (0.15)
SDSS2916	0.1240 (0.0005)	1.24 (0.14)	0.88 (0.03)	0.066 (0.038)	19.937 (0.062)	10.428 (0.401)	-14.37 (0.17)	-10.67 (0.09)	-14.50 (0.15)
SDSS2992	0.1270 (0.0001)	8.87 (0.20)	0.89 (0.02)	0.127 (0.027)	20.034 (0.046)	9.881 (0.301)	...	-12.15 (0.25)	...
SDSS3080	0.1740 (0.0005)	-4.51 (0.12)	1.00 (0.02)	-0.038 (0.023)	20.236 (0.031)	10.710 (0.030)	...	-10.18 (0.26)	...
SDSS3087	0.1650 (0.0005)	-1.26 (0.12)	1.06 (0.02)	0.025 (0.024)	20.266 (0.032)	9.373 (0.089)	...	-12.05 (0.18)	...
SDSS3451	0.2500 (0.0005)	-3.28 (0.22)	1.06 (0.03)	-0.038 (0.029)	20.958 (0.037)	10.824 (0.328)	-10.85 (0.30)	-13.38 (0.59)	-11.00 (0.15)
SDSS3592 <sup>a</sup>	0.0870 (0.0002)	-3.51 (0.08)	0.97 (0.01)	-0.040 (0.021)	18.751 (0.026)	10.395 (0.138)	-18.34 (0.26)	-11.35 (0.17)	-17.40 (0.15)
SDSS3592	0.0870 (0.0002)	0.17 (0.08)	0.97 (0.01)	-0.040 (0.021)	18.751 (0.026)	10.395 (0.138)	-17.14 (0.47)	-11.04 (0.17)	-17.10 (0.15)
SDSS5533	0.2200 (0.0005)	2.29 (0.23)	0.98 (0.03)	0.046 (0.025)	21.173 (0.034)	9.440 (0.183)	-14.17 (0.19)	-10.50 (0.02)	-14.40 (0.15)
SDSS5549	0.1210 (0.0050)	0.29 (0.12)	1.02 (0.01)	0.033 (0.021)	19.654 (0.026)	8.749 (0.132)	...	-10.41 (0.30)	...
SDSS5844	0.3110 (0.0005)	5.03 (0.36)	1.01 (0.05)	-0.099 (0.033)	21.571 (0.051)	9.326 (0.479)	-12.09 (0.12)	-11.10 (0.08)	-12.00 (0.15)
SDSS5957	0.2800 (0.0005)	2.81 (0.26)	0.98 (0.05)	-0.089 (0.033)	21.453 (0.043)	10.232 (0.147)	...	-9.55 (0.19)	...
SDSS6057	0.0670 (0.0001)	3.36 (0.12)	0.94 (0.02)	0.129 (0.026)	18.641 (0.044)	9.944 (0.075)	...	-11.99 (0.49)	...
SDSS6192	0.2720 (0.0005)	5.69 (0.38)	0.83 (0.06)	-0.018 (0.038)	21.698 (0.046)	9.611 (0.567)	...	-9.59 (1.15)	...
SDSS6304	0.1900 (0.0005)	6.04 (0.20)	0.93 (0.04)	0.095 (0.024)	20.952 (0.028)	10.377 (0.116)	-16.59 (0.04)	-11.55 (0.37)	-18.50 (0.15)
SDSS6315 <sup>a</sup>	0.2670 (0.0005)	-0.30 (0.25)	0.97 (0.04)	-0.166 (0.030)	20.919 (0.044)	9.785 (0.430)	-14.71 (0.47)	-12.13 (0.33)	-14.60 (0.15)
SDSS6315	0.2670 (0.0005)	2.66 (0.25)	0.97 (0.04)	-0.166 (0.030)	20.919 (0.044)	9.785 (0.430)	-13.99 (0.28)	-13.25 (0.12)	-14.20 (0.15)
SDSS6699 <sup>a</sup>	0.3110 (0.0005)	-2.38 (0.34)	0.87 (0.07)	-0.126 (0.040)	21.796 (0.049)	10.734 (0.479)	...	-10.18 (1.10)	...
SDSS6699	0.3110 (0.0005)	3.72 (0.34)	0.87 (0.07)	-0.126 (0.040)	21.796 (0.049)	10.734 (0.479)	-12.79 (0.38)	-10.53 (0.09)	-12.90 (0.15)
SDSS6780	0.2020 (0.0050)	9.10 (0.29)	0.79 (0.04)	-0.004 (0.035)	20.947 (0.056)	11.170 (0.221)	...	-11.78 (0.38)	...
SDSS6933	0.2130 (0.0050)	0.44 (0.17)	0.99 (0.03)	0.002 (0.025)	20.832 (0.030)	8.975 (0.866)	...	-11.28 (0.16)	...
SDSS6936	0.1810 (0.0005)	-0.34 (0.21)	1.00 (0.03)	-0.007 (0.025)	20.575 (0.031)	10.365 (0.242)	-10.93 (0.22)	-10.34 (0.22)	-10.90 (0.15)
SDSS7147 <sup>a</sup>	0.1100 (0.0005)	-1.32 (0.14)	0.80 (0.02)	-0.034 (0.026)	19.516 (0.030)	10.310 (0.023)	...	-7.79 (0.04)	...
SDSS7147	0.1100 (0.0005)	0.40 (0.14)	0.80 (0.02)	-0.034 (0.026)	19.516 (0.030)	10.310 (0.023)	...	-10.66 (0.08)	...
SDSS7475	0.3220 (0.0050)	3.07 (0.33)	1.02 (0.06)	-0.123 (0.033)	21.535 (0.042)	8.949 (1.337)	-10.00 (0.53)	-9.48 (0.15)	-9.50 (0.15)
SDSS7512	0.2190 (0.0050)	-1.58 (0.23)	1.05 (0.04)	0.027 (0.030)	21.104 (0.044)	9.888 (0.106)	-15.22 (0.28)	...	-15.00 (0.15)
SDSS7847	0.2120 (0.0005)	-1.42 (0.24)	1.02 (0.04)	0.155 (0.028)	21.225 (0.033)	10.314 (0.112)	-20.81 (0.43)	-15.87 (0.61)	-20.20 (0.15)
SDSS8046	0.2590 (0.0005)	-3.32 (0.30)	1.05 (0.05)	0.077 (0.038)	21.633 (0.044)	11.196 (0.106)	-20.16 (0.35)	-10.34 (0.11)	-19.00 (0.15)
SDSS10434	0.1040 (0.0005)	2.52 (0.22)	1.01 (0.03)	-0.053 (0.029)	19.185 (0.042)	10.955 (0.128)	-11.06 (0.23)	-10.23 (0.34)	-10.80 (0.15)
SDSS11864	0.3030 (0.0005)	3.62 (0.79)	1.01 (0.17)	0.070 (0.063)	22.299 (0.076)	9.270 (0.301)	...	-10.80 (0.24)	...
03D1ax	0.4960 (0.0010)	-2.17 (0.09)	0.93 (0.01)	-0.062 (0.028)	22.992 (0.035)	11.580 (0.112)	-9.56 (0.22)	-6.44 (0.00)	-9.80 (0.15)
03D1dt	0.6120 (0.0020)	7.26 (0.69)	1.05 (0.07)	-0.054 (0.040)	23.300 (0.047)	9.715 (0.092)	-12.86 (2.25)	...	-13.20 (0.15)
03D1ew	0.8680 (0.0010)	2.15 (0.40)	1.04 (0.04)	-0.036 (0.054)	24.359 (0.072)	8.530 (0.805)	-18.22 (0.06)	...	-18.90 (0.15)
03D3bl	0.3553 (0.0005)	3.58 (0.32)	1.00 (0.03)	0.241 (0.026)	22.951 (0.032)	10.831 (0.093)	-15.91 (0.00)	-10.48 (0.24)	-16.70 (0.15)
03D4at	0.6340 (0.0010)	5.84 (0.38)	1.02 (0.04)	-0.008 (0.053)	23.733 (0.047)	8.751 (0.078)	-15.49 (0.63)	...	-16.80 (0.15)
03D4cx	0.9490 (0.0140)	2.76 (0.55)	0.95 (0.07)	0.019 (0.055)	24.464 (0.082)	11.008 (0.157)	-17.04 (0.22)	...	-17.80 (0.15)
04D1dc	0.2110 (0.0010)	-1.71 (0.21)	0.86 (0.02)	0.023 (0.021)	21.084 (0.026)	10.635 (0.041)	-13.94 (0.02)	-11.20 (0.27)	-13.80 (0.15)
04D1hx	0.5600 (0.0020)	5.29 (0.20)	1.04 (0.02)	0.143 (0.033)	23.715 (0.039)	9.645 (0.133)	-14.27 (0.08)	...	-15.00 (0.15)
04D1ow <sup>a</sup>	0.9150 (0.0140)	3.56 (0.18)	1.00 (0.03)	-0.124 (0.044)	24.366 (0.070)	9.397 (1.373)	-9.38 (0.29)	...	-8.70 (0.15)
04D1ow	0.9150 (0.0140)	6.06 (0.18)	1.00 (0.03)	-0.124 (0.044)	24.366 (0.070)	9.397 (1.373)	-11.11 (0.65)	...	-10.50 (0.15)
04D1pd	0.9500 (0.0200)	1.92 (0.35)	1.04 (0.05)	0.022 (0.050)	24.734 (0.078)	10.215 (0.115)	-12.61 (5.38)	...	-12.60 (0.15)
04D1pp	0.7350 (0.0010)	1.68 (0.20)	0.87 (0.03)	-0.064 (0.042)	23.998 (0.049)	11.382 (0.090)	-13.89 (0.27)	...	-14.00 (0.15)
04D1sk	0.6634 (0.0005)	-0.58 (0.31)	1.03 (0.04)	0.100 (0.044)	24.058 (0.046)	10.416 (0.150)	-23.36 (0.34)	...	-23.00 (0.15)
04D2an	0.6200 (0.0190)	-3.52 (0.46)	0.99 (0.08)	-0.019 (0.046)	23.597 (0.046)	7.542 (0.574)	-16.14 (0.40)	...	-15.50 (0.15)
04D2cf	0.3690 (0.0020)	7.74 (1.36)	0.88 (0.05)	0.015 (0.030)	22.491 (0.065)	10.809 (0.157)	-10.95 (0.19)	...	-10.00 (0.15)
04D2fp	0.4150 (0.0020)	2.13 (0.15)	1.03 (0.02)	-0.012 (0.025)	22.559 (0.034)	10.235 (0.218)	-17.19 (0.11)	...	-17.70 (0.15)
04D2fs	0.3570 (0.0020)	1.99 (0.14)	1.01 (0.02)	0.081 (0.023)	22.437 (0.031)	8.386 (0.294)	-19.26 (0.13)	-13.30 (0.08)	-20.00 (0.15)
04D2gp	0.7320 (0.0010)	2.84 (0.36)	0.85 (0.04)	-0.091 (0.064)	24.219 (0.063)	8.834 (0.230)	-17.79 (0.11)	...	-18.70 (0.15)
04D2mc	0.3480 (0.0010)	6.31 (0.11)	0.84 (0.02)	0.142 (0.028)	22.580 (0.040)	10.960 (0.118)	...	-10.37 (0.24)	...
04D3cp	0.8300 (0.0200)	5.74 (0.17)	1.05 (0.03)	-0.180 (0.046)	24.111 (0.060)	10.679 (0.326)	-10.59 (0.36)	...	-9.80 (0.15)
04D3ez	0.2630 (0.0005)	1.29 (0.12)	0.89 (0.02)	0.089 (0.020)	21.697 (0.026)	10.290 (0.012)	-15.89 (0.22)	-9.42 (0.38)	-16.10 (0.15)
04D3mk	0.8130 (0.0010)	-1.69 (0.18)	0.95 (0.03)	-0.104 (0.046)	24.294 (0.058)	9.719 (0.349)	-11.43 (0.07)	...	-11.50 (0.15)
04D3nh	0.3402 (0.0002)	4.50 (0.10)	1.06 (0.02)	0.009 (0.020)	22.142 (0.029)	9.356 (0.021)	...	-12.02 (0.38)	...
04D4ju	0.4720 (0.0010)	-2.63 (0.22)	1.05 (0.03)	0.184 (0.032)	23.771 (0.035)	9.239 (0.177)	-16.43 (1.20)	...	-15.90 (0.15)
05D1cb	0.6320 (0.0010)	5.09 (0.23)	0.97 (0.03)	-0.001 (0.034)	23.715 (0.043)	10.111 (0.079)	-10.43 (0.07)	...	-9.70 (0.15)
05D1ke	0.6900 (0.0100)	2.60 (0.21)	1.04 (0.03)	-0.077 (0.039)	23.611 (0.044)	8.851 (0.333)	-12.05 (0.67)	...	-12.00 (0.15)
05D2ab	0.3230 (0.0010)	-1.26 (0.14)	0.99 (0.02)	-0.013 (0.020)	22.001 (0.030)	10.098 (0.080)	...	-11.29 (0.15)	...
05D2ah	0.1840 (0.0010)	-2.08 (0.10)	0.99 (0.02)	0.019 (0.020)	20.765 (0.025)	9.210 (0.014)	...	-11.37 (0.11)	...
05D2ci	0.6300 (0.0010)	7.42 (0.17)	0.90 (0.03)	0.045 (0.054)	23.612 (0.058)	10.977 (0.159)	-15.82 (1.23)	...	-17.90 (0.15)
05D2dt	0.5740 (0.0040)	-1.61 (0.22)	1.02 (0.04)	0.045 (0.039)	23.656 (0.047)	10.244 (0.096)	-14.44 (0.05)	...	-14.20 (0.15)
05D2he	0.6075 (0.0005)	4.15 (0.33)	1.04 (0.04)	0.073 (0.037)	23.953 (0.044)	9.418 (0.185)	-14.11 (0.37)	...	-14.60 (0.15)
05D2le	0.7002 (0.0005)	6.89 (0.22)	1.05 (0.03)	-0.012 (0.042)	23.961 (0.050)	8.033 (0.690)	-12.39 (0.51)	...	-12.40 (0.15)
05D2nn	0.8700 (0.0200)	-0.29 (0.34)	0.88 (0.06)	-0.147 (0.056)	24.395 (0.086)	12.073 (0.487)	-13.95 (0.40)	...	-13.90 (0.15)
05D3lb	0.6473 (0.0004)	-0.61 (0.18)	1.04 (0.02)	0.035 (0.039)	23.896 (0.043)	8.931 (0.230)	-19.32 (0.09)	...	-19.10 (0.15)
05D3mn	0.7600 (0.0010)	2.80 (0.22)	0.99 (0.03)	-0.021 (0.042)	24.043 (0.048)	10.432 (0.115)	-12.98 (0.33)	...	-13.10 (0.15)
05D3mq	0.2460 (0.0010)	8.30 (0.15)	0.91 (0.03)	0.034 (0.025)	21.521 (0.032)	10.723 (0.076)	...	-10.45 (0.17)	...
05D3ne	0.1692 (0.0002)	-4.01 (0.09)	0.81 (0.03)	-0.147 (0.031)	20.251 (0.041)	11.133 (0.162)	...	-11.32 (0.16)	...
05D4cw	0.3750 (0.0010)	7.25 (0.14)	0.91 (0.01)	-0.120 (0.022)	22.145 (0.031)	10.503 (0.072)	-11.14 (0.28)	-9.89 (0.28)	-10.40 (0.15)

TABLE 2  
HIGH-REDSHIFT SPECTROSCOPY SAMPLE

05D4dw	0.8550 (0.0010)	5.11 (0.31)	1.05 (0.04)	0.008 (0.049)	24.438 (0.071)	9.994 (0.179)	-12.56 (0.42)	...	-12.6
05D4fg	0.8390 (0.0010)	0.39 (0.22)	1.02 (0.03)	-0.102 (0.046)	24.195 (0.058)	11.277 (0.091)	-11.84 (0.13)	...	-11.8
05D4fo	0.3730 (0.0010)	-5.65 (0.07)	0.92 (0.01)	-0.022 (0.020)	22.463 (0.031)	8.381 (0.366)	...	-11.19 (0.27)	...
06D2bk	0.4990 (0.0010)	0.94 (0.28)	1.05 (0.04)	0.036 (0.036)	23.273 (0.039)	8.617 (0.086)	-14.88 (0.21)	...	-15.0
06D2cc	0.5320 (0.0010)	3.73 (0.33)	0.94 (0.04)	0.089 (0.046)	23.468 (0.050)	10.870 (0.108)	-14.26 (0.23)	...	-14.7
06D2fb	0.1242 (0.0004)	1.80 (0.14)	0.96 (0.02)	-0.004 (0.020)	19.772 (0.023)	9.740 (0.124)	-15.85 (0.40)	...	-16.2
06D3fp	0.2680 (0.0010)	-0.11 (0.11)	1.00 (0.02)	0.104 (0.019)	21.748 (0.026)	9.550 (0.259)	...	-11.12 (0.27)	...
06D3gh	0.7200 (0.0050)	-3.22 (0.22)	1.03 (0.04)	-0.021 (0.052)	23.926 (0.056)	9.300 (0.244)	-15.34 (0.05)	...	-14.9
06D4cq	0.4110 (0.0010)	-0.25 (0.10)	1.04 (0.01)	-0.005 (0.020)	22.562 (0.031)	9.107 (0.088)	-16.80 (0.15)	...	-16.7

NOTE. — Uncertainties shown in parentheses.

<sup>a</sup> Spectrum not used to determine adopted maximum-brightness ejecta velocity.